Journal of Molecular Modeling (2019) 25: 336
https://doi.org/10.1007/s00894-019-4233-y

ORIGINAL PAPER

In silico characterization of residues essential for substrate binding of human cystine transporter, xCT

Monika Sharma [1] · C. R. Anirudh [1]

Received: 1 May 2019 / Accepted: 14 October 2019 / Published online: 9 November 2019

Abstract

xCT is a sodium-independent amino acid antiporter that imports L-cystine and exports L-glutamate in a 1:1 ratio. It is a component of heterodimeric amino acid transporter system Xc- working at the cross-roads of maintaining neurological processes and regulating antioxidant defense. The transporter has 12 transmembrane domains with intracellular N- and C-termini, and like other transporter proteins can undergo various conformational changes while switching the ligand accessibilities from intracellular to extracellular site. In the present study, we generated two homology models of human xCT in two distinct conformations: inward-facing occluded state and outward-facing open state. Our results indicated the substrate translocation channel composed of transmembrane helices TMs 1, 3, 6, 8, and 10. We docked anionic L-cystine and L-glutamate within the cavities to assess the two distinct binding scenarios for xCT as antiporter. We also assessed the interactions between the ligands and transporter and observed that ligands bind to similar residues within the channel. Using MM-PBSA/MM-GBSA approach, we computed the binding energies of these ligands to different conformational states. Cystine and glutamate bind xCT with favorable binding energies, with more favorable binding observed in inward occluded state than in outward open state. We further computed the residue-wise decomposition of these binding energies and identified the residues as essential for substrate binding/permeation. Filtering the residues that form favorable energetic contributions to the ligand binding in both the states, our studies suggest T56, A60, R135, A138, V141, Y244, A247, F250, S330, L392, and R396 as critical residues for ligand binding as well as ligand transport for any conformational state adopted by xCT during its transport cycle.

Keywords Human cystine transporter · Homology modeling · Binding energies · Transmembrane proteins

Introduction

The cystine-glutamate transporter (xCT) is a component of heteromeric, sodium-independent amino acid transport (HAT) system, Xc-, with high specificity for cystine and glutamate [1, 2]. The function of Xc- primarily connects neurotransmission and behavior with the antioxidant defense [3–5]. System Xc- includes specific light chain transporter xCT (~ 40 kDa) and heavy chain, 4F2hc (~ 80 kDa), which are linked by a disulfide bridge [6, 7]. In a functional dimer, 4F2hc is responsible for trafficking of the light chain and xCT is required for the transport activity of the dimer. Reconstitution studies on similar HAT system (SLC7A9) showed that light chains, xCT, are fully functional in the absence of its corresponding heavy subunit (4F2hc) [8]. Expression of xCT on the cell membrane is essential for the uptake of cystine required for intracellular glutathione (GSH) synthesis and maintaining the intracellular redox balance [9]. Extracellular glutamate acts as a competitive inhibitor for cystine uptake via system Xc-, indicating that xCT primarily imports anionic cystine and exports glutamate in 1:1 ratio as an electroneutral antiporter exchange system for cystine/glutamate [10]. Impairment of xCT results in disruption in glutamate homeostasis as observed in primary gliomas, resulting in elevated glutamate secretion and neuronal cell death [11–13]. Dysfunction of xCT or decreased levels of mRNA expression of SLC7A11, gene associated with encoding xCT, has been linked with various

Electronic supplementary material The online version of this article (https://doi.org/10.1007/s00894-019-4233-y) contains supplementary material, which is available to authorized users.

✉ Monika Sharma
mnsharma@iisermohali.ac.in

[1] Department of Chemical Sciences, Indian Institute of Science Education and Research (IISER), Sector 81, Knowledge City, SAS, Nagar, Punjab, India

neurodegenerative disorders [5, 14, 15], such as schizophrenia [16], amyotrophic lateral sclerosis (ALS) [17], multiple sclerosis (MS) [18], and Parkinson's diseases [19]. On the other hand, xCT is upregulated in various cancer cell lines under oxidative stress including pancreatic cancer [20], breast cancer [21, 22], bladder carcinoma cells [23], and lung tumor progression [24]. Expression of xCT has also been proposed as a predictor of disease recurrence in patients with colorectal cancer [25]. Enhanced biosynthesis of intracellular GSH via xCT protects cancer cells from drug-induced oxidative stress by mediating drug detoxification or inactivation [26–28]. In addition, xCT has been identified as the predominant mediator of Kaposi's sarcoma-associated herpesvirus (KSHV) fusion and entry permissiveness into cells [29–31]. These findings make xCT a promising therapeutic target in cancer therapy [32–35] and in neurodegenerative or neuroinflammatory diseases [3, 5, 36, 37].

A detailed molecular understanding of conformational transitions of xCT during the substrate transport would offer new opportunities for drug discovery [38, 39]. This warrants the need to have structural information of human cystine transporter. There have been structural experimental studies [40–42] indicating that xCT is a protein with 12 transmembrane (TM) helices, both N- and C-termini located intracellularly, and re-entrant loop between helices TM2 and TM3 that participate in substrate permeation. The only structures available till date are two homology models. One model was constructed using ApcT crystal structure [14]. Another xCT modeled structure was reported recently [43] where human xCT structure was mapped onto the modeled structure of homologous fungal cystine transporter, CgCYN1. With the advancement in membrane structural biophysics and crystallography, the transporters have been captured in different conformational states, suggesting that there are several conformational states accessible to these transporters as they switch accessibility from one side of the membrane to the other [44–52], and are now thought to operate by a common "alternating access" model [53, 54]. This implies that there are many fundamental questions that are open to investigate further about xCT. More detailed investigations of structural rearrangements of transporters at atomic level have been made possible by molecular dynamics simulations [55–61]. In this study, we combined homology modeling, ligand docking, and molecular dynamics simulation technique to investigate the ligand binding, and identified the residues which are involved in ligand binding. We constructed homology models of xCT in two distinct conformations as adopted by their template structures: inward-facing occluded state and outward-facing open state. The inward-facing occluded state of xCT is modeled using ApcT structure (PDBid:3GIA) (hereafter referred as Model_Cioc), and the outward-facing open state of xCT is modeled using AdiC structure (PDBid:5J4I) (hereafter referred as Model_Cout) as templates. These models were refined using molecular dynamics simulations and docked with cognate ligands: anionic cystine and glutamate. The latter is done to investigate the fact that similar uptake specificities are observed for both L-cystine and L-glutamate which suggests that the similar residues within the transmembrane region are involved in binding these cognate ligands. We then explored contributions of each residue to the overall binding free energy using MM-PB(GB)/SA method. Our aims for this study are threefold: (i) modeling of xCT is two different conformational states; (ii) probable ligand binding sites for these states; and (iii) identification of residues essential for ligand binding.

Methods

Identification and modeling of transmembrane (TM) region of xCT

Human xCT sequence was retrieved from NCBI, and an initial topology prediction was carried out using Constrained Consensus TOPology (CCTOP) server [62], which utilizes ten topology prediction methods: HMMTOP, MemBrain, Memsat, Octopus, Philius, Phobius, Pro, Prodiv, Scampi, ScampiMsa, and TMHMM in combination with the topology information from PDBTM, TOPDB, and TOPDOM databases using the probabilistic framework of hidden Markov model. xCT was predicted to be a 12-transmembrane helical protein with N- and C-termini located inside the cell. Sequence spanning transmembrane region (residues 45 to 512) was submitted to HHPred server against PDB structures for homology detection, and two templates, ApcT (PDbid:3GIA) [63] and AdiC (PDbid:5J4I)[64] were selected using HHblits multiple sequence alignment method [65]. Transmembrane region of xCT showed ~ 26.17% and 24.28% sequence identity with ApcT (E value:2e-16) and AdiC (E value:3e-15), respectively (Fig. 1). These two structures are in different conformational states of their transport cycle.

AdiC arginine antiporter is reported in substrate-free outward-facing state [64], and ApcT is reported in substrate-free inward-facing occluded open state [63]. The only inward open conformation known for any wild-type amino acid transporter is that of GadC [66]. However, the reported structure consists of C-terminal fragment (C-plug) whose displacement is requisite for GadC transport activity. There is no report suggesting importance of similar C-plug in xCT. Thus, we decided not to opt for GadC as template for this study. Comparative modeling of TMD region of xCT spanning residues 45 to 512 including TMD helices and connecting loops was carried out based on multiple sequence alignment of these two templates using Modeller9v15 [67]. Two representative models corresponding to the two templates were selected from the

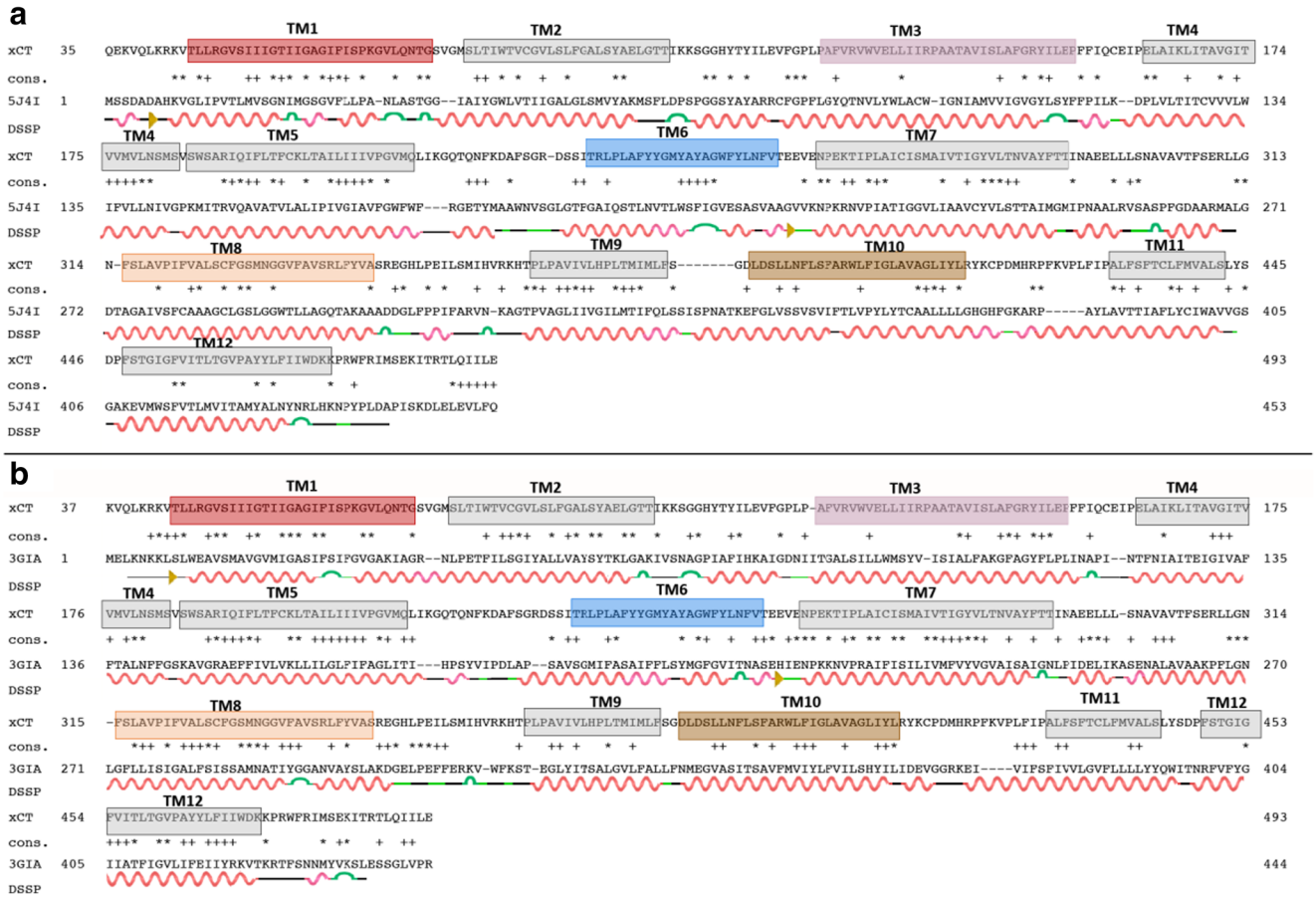

Fig. 1 Sequence alignment of transmembrane region of xCT with respect to the template structures of A. AdiC (PDbid:5J4I) and B. ApcT (PDbid:3GIA) used for homology modeling. The proposed transmembrane helices are highlighted as blocks. The secondary structure elements as indicated by DSSP analysis of the template structures are also shown alongside the template sequence

collection of 5000 models built by Modeller, based on the evaluation of discrete optimized protein energy (DOPE) potential. The models were further subjected to loop refinement module of Modeller9v15 to refine the connecting intracellular and extracellular loops, and energetically favorable models were selected among the 1000 generated models based on the DOPE score. Thus, two models of xCT have been generated using two different templates in different conformational states of access cycle herein referred as Model_Cioc (template structure: 3GIA) and Model_Cout (template structure: 5J4I).

Minimization and refinement of modeled structure using MD in explicit membrane

The selected models were minimized further to obtain stable structures using molecular dynamics simulations. Simulation setup with model inserted into a heterogeneous fully hydrated bilayer of size 85 Å × 85 Å, consisting of lipids as well as cholesterol molecules, was obtained using CHARMM-GUI [68] using CHARMM36m force fields [69] for lipids as well as protein. Prior to membrane insertion, we calculated rotational and translational positions of xCT models in membranes using PPM server [70], and the obtained orientation was used for positioning within lipid bilayer in CHARMM-GUI. The constituents of lipid bilayer were selected in order to mimic the human brain barrier membrane environment [71] DPPC(5%):POPC(20%):POPE(15%):POPS(5%):POPI(5%):-PSM(30%) lipids with cholesterol (20%). The structures were then solvated with TIP3P water molecules, followed by the addition of K^+ and Cl^- ions for 0.15 M concentration. The assembled simulation system consisted of ~ 90,000 atoms. The biomolecular systems were simulated using NAMD2.11 [72]. Minimization was carried out for 10000 steps, and system was equilibrated for 0.5 ns, while slowly releasing the collective variable restraints to facilitate stable simulation. Finally, structure was further simulated without any restraints for 10 ns at a constant temperature of 303 K using Langevin thermostat with damping coefficient of 1 ps^{-1}, and constant pressure of 1 atm using semi-isotropic Nose-Hoover Langevin piston pressure control with oscillation period of 0.05 ps and oscillation decay time of 0.025 ps. The van der Waals interactions were smoothly switched off at 10–12 Å by a force-switching function, and long-range electrostatic interactions were calculated using particle mesh Ewald method [73]. All

bond lengths involving hydrogen atoms were fixed using SHAKE algorithm, enabling the use of 2 fs time step. The final obtained structures were validated with a new Cβ measure and updated Ramachandran plot as described in [74] and implemented in RAMPAGE (http://www-cryst.bioc.cam.ac.uk/rampage). The refined models were then used for docking purposes, and the models with docked ligands (eight xCT conformations in total) were simulated for 100 ns each, resulting in simulation data used in the study as 800 ns.

Docking of modeled structures with ligands: L-cystine or L-glutamate

For ligands, coordinates for anionic L-cystine and L-glutamate were obtained from PubChem database (https://pubchem.ncbi.nlm.nih.gov) in sdf format. Binding site analysis was done by docking using AutodockVina [75], a computational docking program installed as plugin in PyMol [76]. Prior to docking, pore dimensions within the representative structures were analyzed using HOLE program [77]. The docking box sizes for each model were selected such that the cylindrical cavity was covered within the box volumes of ~ 30 Å × 30 Å × 30 Å enclosing the probable binding pocket. The residues within the binding pocket were defined as flexible residues to accommodate the ligands. Based on unique binding pose and favorable Vina docked score, two best docked conformations were selected per conformational state, and subjected to molecular dynamics. The eight docked xCT conformations were embedded in lipid bilayer as discussed above and simulated using similar protocol (as adopted for modeled structures) for 100 ns. Parameters for anionic cystine and glutamate were obtained for ligand generator module [78] of Charmm-GUI.

Trajectory analyses of protein-ligand complexes

Structural analyses were done using VMD-1.9.3 [79]. Root mean square deviations for the backbone atoms were calculated with reference to the refined modeled structure. Root mean square fluctuations (RMSF) of Cα atoms in all the trajectories were also calculated. Pore radius profiles of the transporter pathway were calculated using HOLE program [77, 80]. A total of 50000 snapshots of protein atoms were extracted from the simulation data at equal interval and submitted to HOLEtraj wrapper [81] available with MDAnalysis 0.19.2 [82].

Interactions of ligands with protein

All the ligand docked conformations sampled at every 2 ps for eight trajectories were pooled in to visualize protein-ligand interactions in ligand docked conformations. Interaction of ligand with protein residue was defined when heavy atom of ligand interacts with protein residue within cutoff distance of 5.0 Å. Variations in interactions between ligands and protein residues were analyzed using VMD1.9.3 [79]. The docked conformations were clustered into five clusters using *kmeans* algorithm implemented in *cpptraj* [83].

MM-PB(GB)/SA-based binding affinities

MM-PB(GB)/SA is a force field–based method to approximate the free energies of binding based on ensemble of conformations obtained from MD simulations [84, 85]. This method employs molecular mechanics, Generalized Born (GB) or Poisson Boltzmann (PB) solvation models, and solvent accessibility method. The binding free energy ΔG_{bind} is estimated from the free energies of the reactants and product of the reaction: $\Delta G_{\text{bind}} = \langle G_{\text{PL}} \rangle - \langle G_{\text{P}} \rangle - \langle G_{\text{L}} \rangle$

where free energy of state (P/L/PL) is estimated as sum of terms:

$$G = E_{\text{bonded}} + E_{\text{el}} + E_{\text{vdw}} + G_{\text{pol}} + G_{\text{np}} - \text{TS}$$

The first three terms are standard molecular mechanics energy terms associated with bonded (bond, angle, and dihedral), electrostatic, and van der Waals interaction. G_{pol} and G_{np} are polar and non-polar contributions to solvation free energies. G_{pol} is obtained by solving PB or GB model equation, and G_{np} is estimated from solvent accessibilities values. T and S are absolute temperature and entropy estimated by normal mode analysis of vibrational frequencies. An ensemble of 50000 snapshots of xCT structures bound with ligands per trajectory were obtained at equal intervals and used for calculating binding free energies using MMPBSA.py available in Amber16. The binding energy calculations were carried out using both MM-PBSA and MM-GBSA method using CHARMM36m force fields. Per-residue decomposition was also carried out for residues present within 15 Å of ligand. Energy contribution of single residue to the binding energy was calculated by summing its interactions over all residues in the system.

Results

Homology modeled structures of xCT in two distinct conformations of transition cycle

In the absence of a crystal structure of any cystine transporter, we built homology model of human cystine transporter *xCT* based on crystal structures of transporters that were expected to have similar folds. Comparative analysis of xCT sequence using CCTOP server predicted the overall topology of the transporter to consist of 12 transmembrane domains (Fig. S1). Based on the region spanning the transmembrane domain

region (residues 45 to 512), two templates were identified for modeling using HHPred: ApcT (broad-specificity proton-coupled amino acid transporter from *M. jannaschii*) and AdiC (an arginine/agmatine antiporters of *E. coli*) with sequence identity of ~ 26% and ~ 21%, respectively. This was followed by modeling of the transmembrane (TM) region of xCT using Modeller9v15. We further refined the models using simulations, and validated the refined modeled structures using Ramachandran plots [74]. The plots showed above 95% of the residues in favored and allowed regions (Fig. S2). We assessed the local structural quality of our transmembrane protein models (Fig. S3) using qualitative model energy analysis (QMEANBrane) [86]. Both the analyses suggested the reliability of our predicted homology modeled structures in both conformations.

Crystal structures of these two transporters have similar structural core LeuT type-fold of APC transporters which consists of two intertwined 5-TM-helix repeats (TMs 1–5 and TMs 6–10) sharing a twofold inverted pseudo symmetry [87]. The two templates are in different conformational state of substrate transport cycle. ApcT structure is reported in substrate-free inward-facing occluded conformation in PDbid:3GIA. AdiC is reported in substrate-free outward-facing state in PDbid:5J4I. The overall structure of xCT modeled on the above two templates reveals an overall cylindrical shape with 12 transmembrane helices with short extracellular and cytoplasmic loops and intracellular amino and carboxy termini (Fig. 2). In two models, the 12 TMs are arranged in two intertwined V-shaped inverted repeating units (TMs 1–5 and TMs 6–10), followed by TMs 11 and 12. Our models are in agreement with the biotinylated experiments that proposed the first topological model for xCT of 12 transmembrane domains with the N- and C-termini located inside the cell [40]. For the inward occluded model, we observe that the intracellular loop IL23 between TM helices 2 and 3 occludes the intracellular site, and this loop is believed to be involved in substrate permeation pathway [40]. The modeled structures were then embedded in heterogeneous lipid bilayer and further refined using unrestrained molecular dynamics simulations. Superposition of the simulated model structures with the templates (Fig. 3) suggests that residues of five transmembrane helices (TM1, TM3, TM6, TM8, and TM10) form the substrate translocation channel and the cylindrical cavity was assessed to be large enough to accommodate the ligands, and therefore, the probable ligand binding sites. The structural analysis of models and positioning of proteins in membrane (PPM server [70]) yielded the length of translocation channel as ~ 16.0 Å. We analyzed the pore dimensions within the modeled structures using HOLE program (Fig. 4) and docked the ligands within the cylindrical cavity lined by the residues from the helices: TM1, TM3, TM6, TM8, and TM10.

Variations and dynamics of ligand bound complexes during simulations

We analyzed changes in root mean square deviations (RMSD) for two regions: the protein backbone atoms of the ligand bound modeled structures (Fig. 5a) and the protein backbone of the transmembrane region with respect to their initial minimized structures (Fig. 5b). The general trend, inferred from the RMSD values, reveals that though there are deviations observed during the simulations in the complete structure, the transmembrane domains remains stable with considerable reduced RMSD values. We carried out analysis of RMSF values for each simulated system (Fig. 5c) and observed that for both conformations, the residues belonging to loops or non-helical regions (as indicated by grey-colored bar regions) show higher fluctuations, and the residues in the helical region

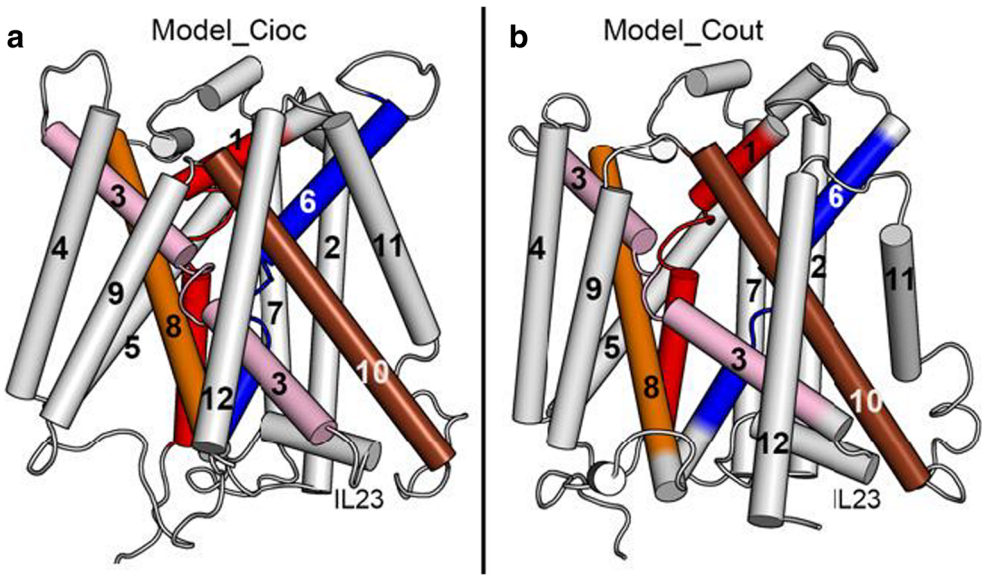

Fig. 2 Homology structure of xCT in **a** inward-facing occluded state Model_Cioc and **b** outward-facing state: Model_Cout. The transmembrane helices are marked and the five helices forming probable translocation channel are shown colored. The intracellular loop IL23 is also shown

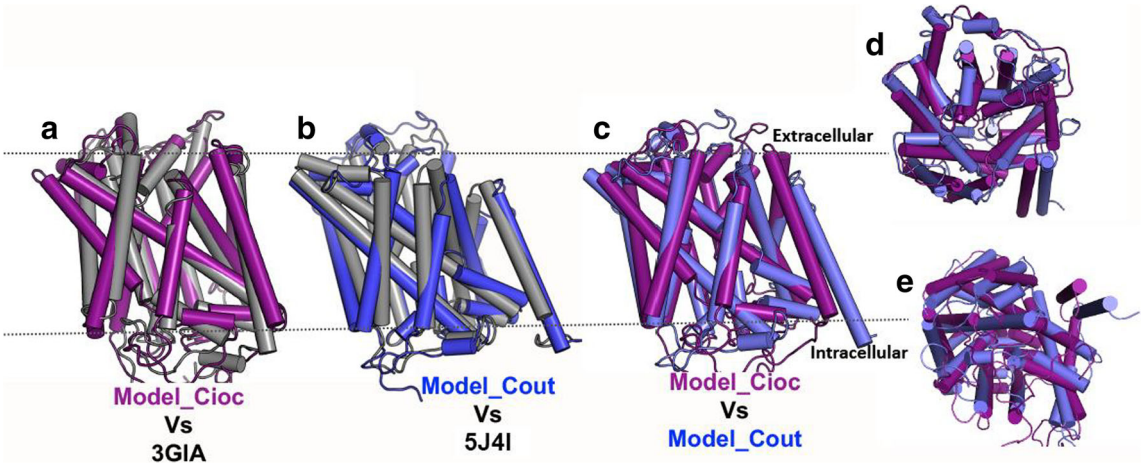

Fig. 3 Alignment of modeled structures obtained after structural refinement with respect to their respective template structures. These xCT structures showed rmsd values of (A) 2.5 Å (with respect to 3GIA) and (B) 2.8 Å (with respect to 5J4I). (C) Structural alignment of the modeled structures showed rmsd values of 4.5 Å. Alignment views of modeled structures are shown from (D) the extracellular side (top view) and (E) the intracellular side (bottom view)

are more stable with significantly less rmsf values. In all simulations, the highest rmsf values are observed for residues belonging to interhelical loop IL5-6 connecting the helices TM5 and TM6.

Pore dimension analyses of ligand bound xCT conformations

We characterized the functional state of the transporters during the simulations by calculating the radius of the translocation pathway in the generate protein conformations using HOLE program (Fig. 6). HOLE employs Monte Carlo-simulated annealing approach to find the best path for a sphere (of variable radius) to squeeze through the channel. The program has been successfully used to analyze the transporter pathways and channels [81, 88–91]. Visualizing the two-dimensional plots of the pore channel radius along the Z-axis obtained for the conformations of proteins, we observed that for Model_Cioc (Fig. 6a), the minimum pore radius increases to ~ 3 Å near the middle of channel towards the intracellular side (near ~ − 10 Å of z-coordinate), indicating the occluded inward conformations for ligand binding. For Model_Cout (Fig. 6b), we observe consistent increase in pore radii towards the extracellular side (positive z coordinate) indicating opened pathway towards extracellular side. The analysis suggests that the transporter conformations in either state are maintained during the simulations.

Energetics of ligand binding to xCT

We simulated the ligand docked xCT conformations and calculated the binding energies of these ligands to the xCT conformations using MM-GBSA and MM-PBSA approach. It is mention-worthy that though the reported binding energies here are not absolute values, these values represent the relative differences in binding of these substrates to two different conformations. Both GB and PB models indicated that cystine and glutamate bind xCT in different conformational states with favorable electrostatic energies ($\Delta E_{\text{electrostatics}}$) and

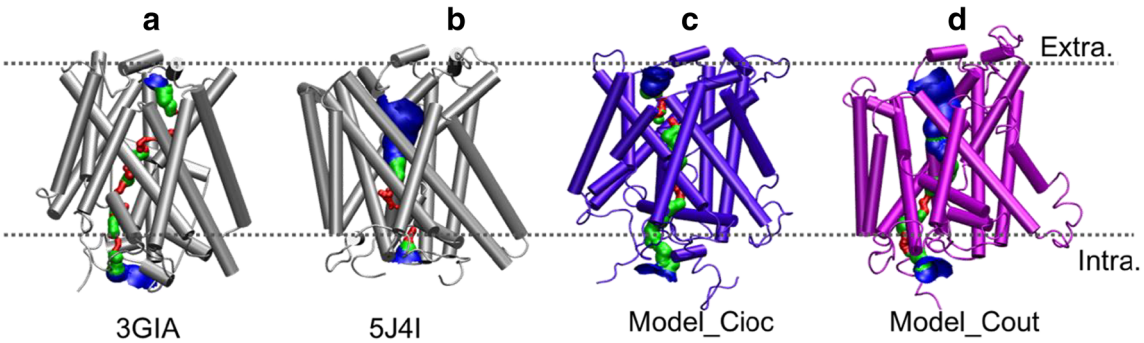

Fig. 4 Visualization of the cavities through the channel of crystal structures used as template (A, B) and modeled structures of xCT (C, D) using HOLE software. Coordinates of modeled structures were obtained after structural refinement using molecular dynamics. Model_Cioc and Model_Cout structures have been modeled using 3GIA and 5J4I as template PDBs. Red-colored area means pore radius below 0.6 Å, green depicts pore radius within range 0.6 to 1.15 Å, and blue-colored depicts pore radius above 1.15 Å

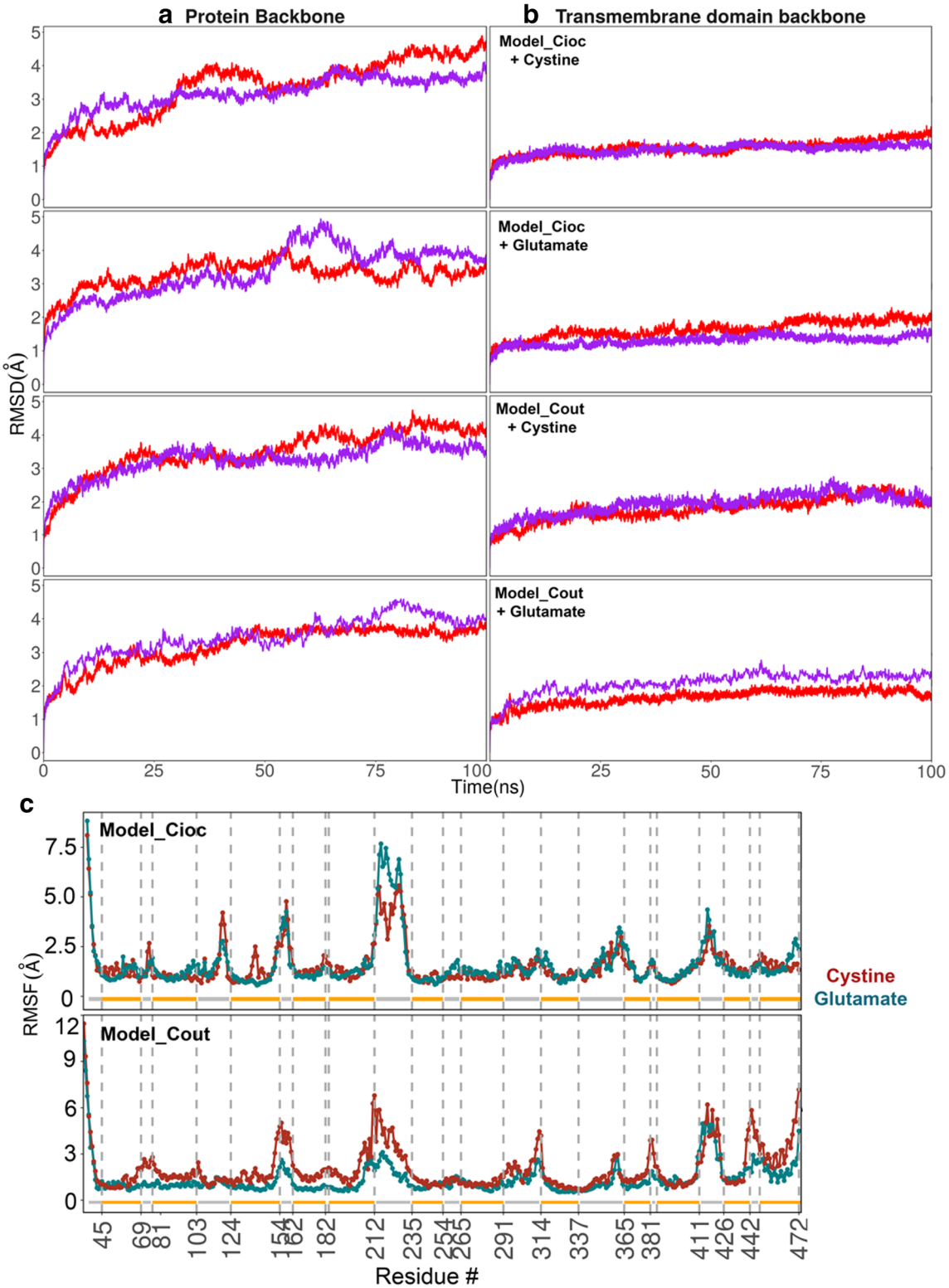

Fig. 5 Root mean square deviation (RMSD) plots of ligand-bound structures with respect to initial minimized modeled structure **a** RMSD values of backbone atoms of complete modeled structures. **b** RMSD values of backbone atoms of transmembrane domains only. Different runs are shown in different colors. **c** Root mean square fluctuations (RMSF) of Cα atoms averaged over multiple simulations. The color bar at the end of plots indicates the secondary structure elements with orange colored helices and grey-colored loops or non-helical regions

unfavorable solvation free energies. The energetic contributions of each interaction are shown in Fig. 7 and the corresponding values are provided in Table SI1. Cystine forms more favorable electrostatics and van der Waals interactions

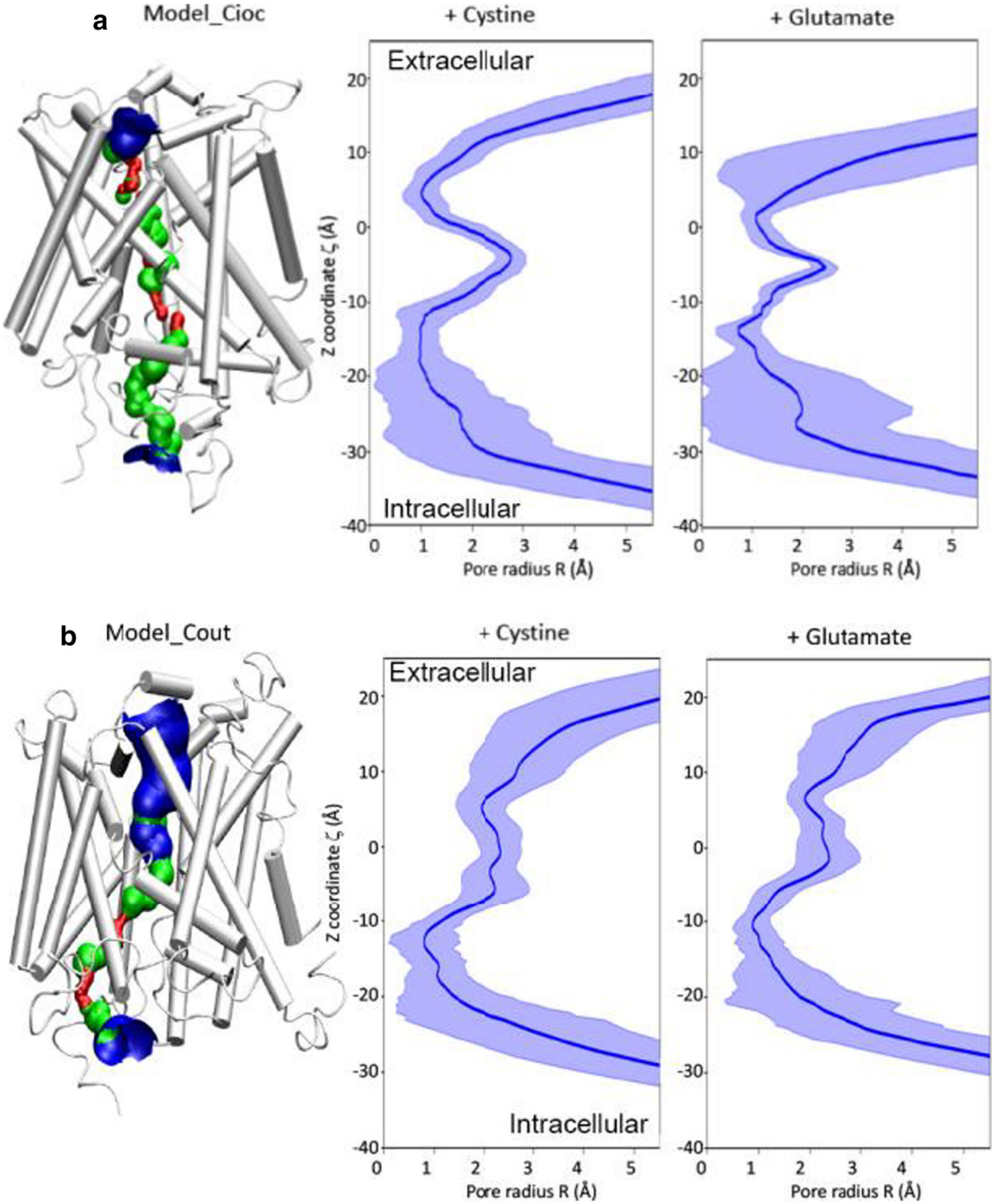

Fig. 6 Functional characterization of conformations of xCT generated during ligand-bound MD simulations **a** in inward-facing occluded state Model_Cioc and **b** in outward-facing state Model_Cout. Pore radii as determined by HOLE are shown along the membrane normal z coordinate with shaded region indicated standard deviation of the radii value from the mean value

with xCT in both inward occluded and outward-facing conformations in comparison with glutamate as suggested by more negative values of $\Delta G_{\text{Binding}}$ obtained via GBSA or PBSA approach. As far as xCT conformational states are concerned, both ligands form favorable interactions with xCT in Model_Cioc (inward-facing occluded) state than with xCT in Model_Cout (outward-facing open) state.

Interactions of cystine in inward-facing occluded and outward open states

Anionic cystine is oxidized dimeric form of cysteine formed by linking two cysteine residues via disulfide bond, and consists of one carboxylate group, one acid group, and two amino groups. The substrate binding site for Model_Cioc is

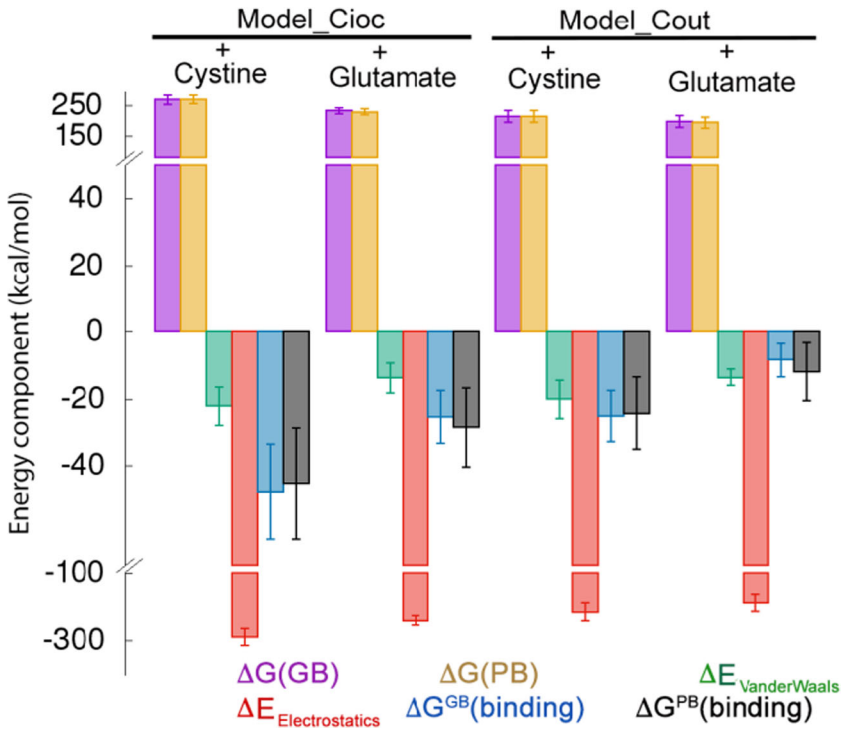

Fig. 7 Binding free energies calculated using MM-GBSA and MM-PBSA approach. $\Delta E_{\text{VanderWaals}}$ and $\Delta E_{\text{electrostatics}}$ correspond to the van der Waals and electrostatics contribution. ΔG_{PB} and ΔG_{GB} correspond to the electrostatic contribution to the solvation free energy calculated by PB or GB, respectively. ΔG_{surf} and $\Delta G_{\text{nonpolar}}$ correspond to the nonpolar contribution to the solvation free energy calculated by empirical model of GB and PB, respectively. $\Delta G_{\text{Binding}}$ is the final estimated binding free energy

approximately halfway across the membrane bilayer, surrounded by residues from five transmembrane helices. We clustered the cystine docked conformations of xCT in different states sampled during the simulations and visualized the interactions within the representative structures (Fig. 8). The representative structures showed cystine to adopt extended conformations within substrate channel of both Model_Cioc and Model_Cout. On one end, the carboxylate

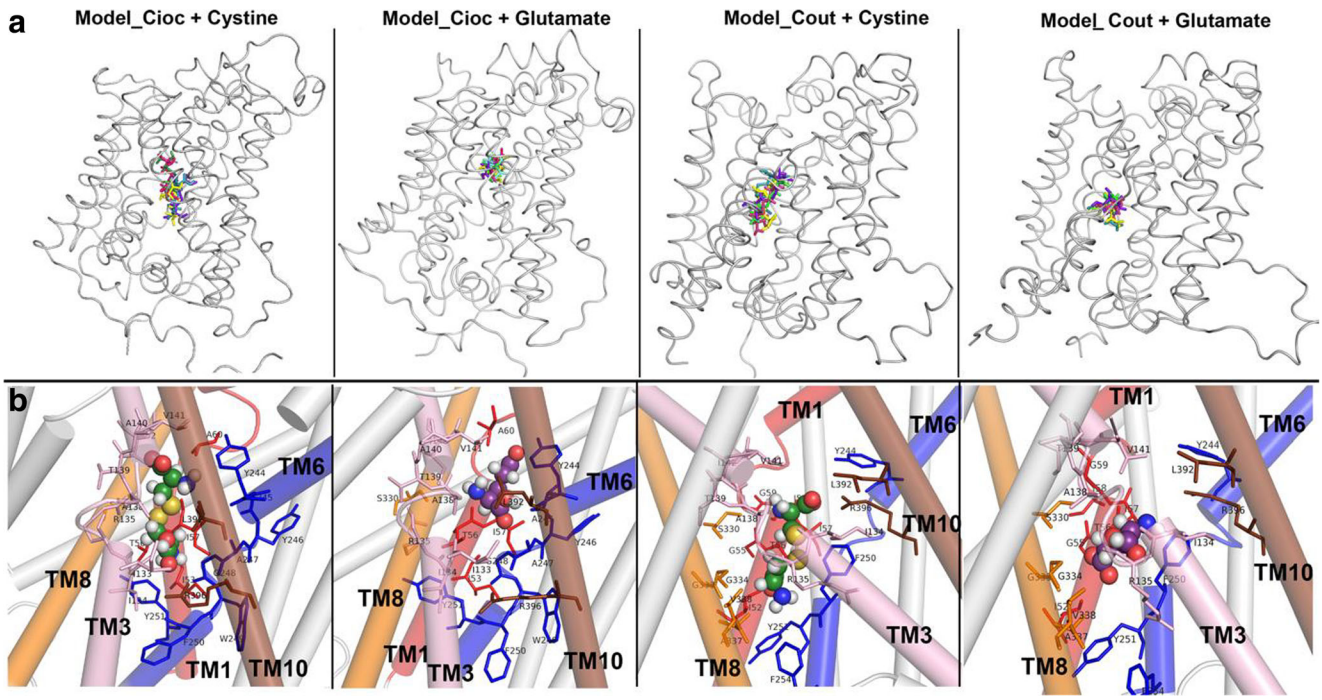

Fig. 8 **a** Conformations of ligands docked inside the transmembrane channel from five representative structures as obtained from kmeans clustering analysis. **b** Close view of the interactions shown for the representative structure corresponding to most populated cluster. The transmembrane helices forming the substrate binding channel are shown in color: TM1: red color; TM3: pink color; TM6: blue color; TM8: orange color; and TM10: brown color

and amino groups of one of the cysteine moieties of the extended cystine molecule forms hydrogen bonds with I134, A140, V141, I142, Y244, and G248. On the other end, carboxylate and amino groups of another cysteine moiety forms hydrogen bonds with R135, G248, W249, F250, Y251, and R396. These interactions are persistently maintained throughout the simulations. In addition, cystine forms persistent hydrophobic interactions with additional residues: I53, T56, I57, A60, I133, I134, A138, T139, A245, Y246, A247, S330, and L392. In outward open conformation (Model_Cout), residues T56, I57, G59, R135, A138, Y244, and R396 form hydrogen bonds with the carboxylate ends of cystine in extended conformation. Cystine is further stabilized via hydrophobic interactions with residues I52, G55, I58, I134, T139, V141, I142, F250, Y251, F254, S330, G333, G334, A337, V338, and L392.

Mapping these interactions with residue-wise decomposed binding energies and relating to the different xCT conformations (Fig. S4), we observed that cystine forms energetically more favorable interactions with the following residues in inward-facing occluded states, than in outward open state: TM1 helix: T56, I57, A60; TM3 helix: R135, T139, A140, V141, I142; TM6 helix: Y244, A245, A247, G248, W249, F250, Y251; TM8 helix: S330; and TM10 helix: L392, S396. Residues in helix TM8 show more significant interactions with cystine in outward open state than in inward occluded state, where residues S330, G333, G334, A337, and V338 form energetically favorable interactions with cystine.

Interactions of glutamate in inward-facing occluded and outward open states

Glutamate as ligand is negatively charged amino acid moiety with two carboxylate groups and one amino group. We analyzed the interactions of glutamate with residues during the docked simulations of inward occluded and outward open xCT conformations (Fig. 8). In Model_Cioc, the terminal carboxylate and amino groups of glutamate substrate form hydrogen bonding interactions with main chains of I58, G59, A60, G61, I62, A247, G248, and side chain hydroxyls of Y244 and Y251. Additional residues T56, I57, A138, V141, I142, A245, Y246, and L392 form hydrophobic interactions with glutamate in inward occluded state. In outward open state (Model_Cout), glutamate forms hydrogen bonding interactions with T56, R135, A137, S330, G333, and G334. Glutamate forms additional interactions with residues I134, A138, V141, F250, A337, V338, L392, and R396 within the ligand channel.

Based on comparative residue-wise decomposition of binding energies for glutamate in different conformational states, the following residues formed energetically favorable interactions with glutamate: TM1 helix: T56, I57, I58, G59, A60, G61; TM3 helix: R135, A138, V141, and I142; TM6 helix: Y244, A245, A247, G248; TM8 helix: S326, S330, M331, G333, G334, F336, A337, V338, R340; and TM10 helix: L392 and R396. The extent of favorable energetic contributions by these residues is higher in inward-facing occluded state than in outward open state. Interestingly, we observed that all the residues belonging to TM3 helix, except R135, contribute less significantly to the binding of glutamate ligand in outward open state (Model_Cout). Similarly, for inward occluded state (Model_Cioc), residues belonging to TM8 helix contribute less to the glutamate binding, except S326 and S330.

Probable amino acids critical for ligand binding

We analyzed the interactions of the cystine and glutamate with the amino acids of xCT and found that similar residues are mostly involved in interacting both anionic cystine and glutamate (Fig. S5). Experimental evidence [41] shows that C327 lies close to substrate permeation pathway, and our results show persistent interactions of ligands with nearby S330 residue of TM8 in both inward occluded and outward open conformations. In our study, we observed that ligands form strong interactions with "$G^{59}A^{60}G^{61}$" motif present in TM1, and these residues contribute significantly to the glutamate binding in inward occluded state. Mutations in similar GXG motifs in other transporters have led to severe defects [92, 93]. Another conserved motif in TM6: "(F/Y)(S/A/T)(F/Y)xGxx" have been identified critical for transporters within APC family [93]. For human xCT, this motif is Y^{244}AYAGWF^{250} present in TM6 and form persistent interactions with both the ligands in both conformational states. Mutagenesis studies on homologous fungal cystine transporter [94] showed transport defect on mutating G255 of TM6 and T339, S340, and H347 of TM8 helix of CgCYN1. Our simulations showed that similar residues belonging to TM6 and TM8 in xCT interact with the ligands.

Discussion

A transporter undergoes various conformational transitions switching accessibility from extracellular site to intracellular site, and simultaneously transporting the ligands. Human xCT is an antiporter that exchanges intracellular glutamate to take up extracellular cystine. Based on its sequence similarity with other transporters whose structures are experimentally derived, we generated two human xCT models in two different conformations: inward-facing occluded state (Model_Cioc) and outward-facing state (Model_Cout). For Model_Cioc, the inward face is observed to be occluded by intracellular loop connecting helices TM2 and TM3. Both models adopted similar fold with 12 transmembrane helices arranged in two intertwined V-shaped inverted repeating units (TMs 1–5 and

TMs 6–10), followed by TMs 11 and 12. Comparative analysis of these models suggested presence of ligand translocation cavity of cylindrical shape formed by five helices TM1, TM3, TM6, TM8, and TM10.

Both the conformational states of xCT were docked with the ligands, and simulated to allow ligands to explore conformational space within the channel. The calculated RMSD and RMSF values suggested transmembrane helical regions to be more stable compared with non-helical regions, as observed from higher fluctuation values in the loop regions. Comparison of pore size profiles as function of membrane normal z for the translocation channel showed that in inward occluded state, there is opening proximal to the intracellular side where ligands can bind. In outward open conformations, the pore radii values increase towards the extracellular side. We computed the binding energies of ligands to xCT in different states and observed that ligands have more favorable binding energies in inward occluded state than in outward-facing state. Anionic cystine binds to xCT in extended conformations and forms more favorable interactions with xCT in either state than those observed with glutamate. We computed residue-wise decomposition of binding energies and observed that in inward-facing occluded state, ligands have favorable interactions with helices TM1, TM3, TM6, and TM10. In outward open state, ligands have favorable interactions with helices TM1, TM3, TM6, and TM8. Interestingly, the energetic contribution of TM1 helical residues to the binding of glutamate is higher than in binding of cystine. Combining the interaction analysis with the decomposed binding energy analysis, we propose a model for ligand transport across the membrane. Our studies suggest that as cystine is transferred from the extracellular site, it enters the channel in extended conformation forming interactions with T56, R135, F250, Y251, R340, and R396 proximal to the intracellular end, and with V141, Y244, and S330 proximal to the extracellular end. Additional interactions are formed with residues belonging to TM8: G333, G334, V335, A337, and V338. Once cystine is inside the channel, and in inward occluded state, it interacts with A60 of TM1, residues at the center of helices TM3 (A138, T139, A140, V141, I142) and TM6 (Y^{244}AYAGWF^{250} motif), S330 of TM8, and L392 and R396 of TM10. Now, as the glutamate is effluxed out of the intracellular site, it forms interactions with R135 (of TM3), S339 (of TM8), and V338, L392, and R396 (of TM10), and as it transfers out to the extracellular site, it interacts with the residues belonging to helix TM1: T56, I57, I58, G59, A60, G61, F63, A64; helix TM3: V141, I142; helix TM6: A247, A245, Y244; and helix TM8: S326 and S330. Filtering the residues that form favorable energetic contributions to the ligand binding in both the states, our studies suggest that residues T56, A60, R135, A138, V141, Y244, A247, F250, S330, L392, and R396 interact with both the ligands as they transport through the channel. Our studies thus identify them as critical residues for ligand binding as well as ligand transport. The fact that similar residues are observed for both the ligands in different conformational states is consistent with the experimental studies where the uptake specificities for these ligands were found to be very similar [1, 10, 95]. To explore the complete scenario, more experimental structures or mutagenesis data is required to investigate further about the substrate binding or transport mechanism of xCT. In the absence of experimental structural studies of xCT, our in silico characterization of critical residues open up possibilities to explore during the structural and biochemical characterization of human cystine transporter.

Conclusion

xCT has been modeled in two different conformations: inward-facing occluded state and outward-facing open state. These states revealed a probable ligand binding cavity lined by residues from five TM helices: TM1, TM3, TM6, TM8, and TM10. The biologically known ligands: cystine and glutamate, were docked within the cavity and observed to have favorable binding energies using MM-PBSA/MM-GBSA approach. Combining results from per residue-wise decomposition of binding energies and interaction analysis, both cystine and glutamate bind to similar set of residues. We identified T56, A60, R135, A138, V141, Y244, A247, F250, S330, L392, and R396 as critical residues for ligand binding as well as ligand transport in xCT. These residues belong to conserved motifs in TM1 and TM6, and map well to the experimentally known important residues important for ligand binding in human xCT or homologous transporter proteins and can form the basis of further residue-specific mutagenesis experiments.

Acknowledgements MS thanks the Department of Science and Technology (DST), India, for INSPIRE Award and research grant (IFA14-CH-165).

Author contributions M.S. conceived, designed, and performed the experiments. A.C.R performed initial experiments. M.S. analyzed the data and wrote the paper. M.S. and A.C.R contributed the literature materials and reviewed the manuscript.

Compliance with ethical standards

Competing interests The authors declare that they have no competing interests.

References

1. Bannai S, Kitamura E (1980) Transport interaction of L-cystine and L-glutamate in human diploid fibroblasts in culture. J Biol Chem 255:2372–2376

2. Makowske M, Christensen HN (1982) Contrasts in transport systems for anionic amino acids in hepatocytes and a hepatoma cell line HTC. J Biol Chem 257:5663–5670
3. Albrecht P, Lewerenz J, Dittmer S et al (2010) Mechanisms of oxidative glutamate toxicity: the glutamate/cystine antiporter system xc- as a neuroprotective drug target. CNS Neurol Disord Drug Targets 9:373–382
4. Domercq M, Sánchez-Gómez MV, Sherwin C et al (2007) System xc- and glutamate transporter inhibition mediates microglial toxicity to oligodendrocytes. J Immunol 178:6549–6556
5. Lewerenz J, Hewett SJ, Huang Y et al (2013) The cystine/glutamate antiporter system xc− in health and disease: from molecular mechanisms to novel therapeutic opportunities. Antioxid Redox Signal 18:522–555. https://doi.org/10.1089/ars.2011.4391
6. Bassi MT, Gasol E, Manzoni M et al (2001) Identification and characterisation of human xCT that co-expresses, with 4F2 heavy chain, the amino acid transport activity system xc. Pflugers Arch 442:286–296
7. Sato H, Tamba M, Kuriyama-Matsumura K et al (2000) Molecular cloning and expression of human xCT, the light chain of amino acid transport system xc. Antioxid Redox Signal 2:665–671. https://doi.org/10.1089/ars.2000.2.4-665
8. Reig N, Chillarón J, Bartoccioni P et al (2002) The light subunit of system b(o,+) is fully functional in the absence of the heavy subunit. EMBO J 21:4906–4914
9. Sato H, Shiiya A, Kimata M et al (2005) Redox imbalance in cystine/glutamate transporter-deficient mice. J Biol Chem 280:37423–37429. https://doi.org/10.1074/jbc.M506439200
10. Bannai S (1986) Exchange of cystine and glutamate across plasma membrane of human fibroblasts. J Biol Chem 261:2256–2263
11. Cho Y, Bannai S (1990) Uptake of glutamate and cysteine in C-6 glioma cells and in cultured astrocytes. J Neurochem 55:2091–2097
12. Kato S, Ishita S, Sugawara K, Mawatari K (1993) Cystine/glutamate antiporter expression in retinal mu¨ller glial cells: Implications fordl-alpha-aminoadipate toxicity. Neuroscience 57:473–482. https://doi.org/10.1016/0306-4522(93)90080-Y
13. Kato S, Negishi K, Mawatari K, Kuo C-H (1992) A mechanism for glutamate toxicity in the C6 glioma cells involving inhibition of cystine uptake leading to glutathione depletion. Neuroscience 48:903–914. https://doi.org/10.1016/0306-4522(92)90278-A
14. Bridges CC, Kekuda R, Wang H et al (2001) Structure, function, and regulation of human cystine/glutamate transporter in retinal pigment epithelial cells. Invest Ophthalmol Vis Sci 42:47–54
15. Lin C-H, Lin P-P, Lin C-Y et al (2016) Decreased mRNA expression for the two subunits of system xc(-), SLC3A2 and SLC7A11, in WBC in patients with schizophrenia: evidence in support of the hypo-glutamatergic hypothesis of schizophrenia. J Psychiatr Res 72:58–63. https://doi.org/10.1016/j.jpsychires.2015.10.007
16. Fournier M, Monin A, Ferrari C et al (2017) Implication of the glutamate–cystine antiporter xCT in schizophrenia cases linked to impaired GSH synthesis. NPJ Schizophr 3:31. https://doi.org/10.1038/s41537-017-0035-3
17. Mesci P, Zaïdi S, Lobsiger CS et al (2015) System xC- is a mediator of microglial function and its deletion slows symptoms in amyotrophic lateral sclerosis mice. Brain 138:53–68. https://doi.org/10.1093/brain/awu312
18. Pampliega O, Domercq M, Soria FN et al (2011) Increased expression of cystine/glutamate antiporter in multiple sclerosis. J Neuroinflammation 8:63. https://doi.org/10.1186/1742-2094-8-63
19. Massie A, Schallier A, Mertens B et al (2008) Time-dependent changes in striatal xCT protein expression in hemi-Parkinson rats. Neuroreport 19:1589–1592. https://doi.org/10.1097/WNR.0b013e328312181c
20. Lo M, Ling V, Wang YZ, Gout PW (2008) The x_c^- cystine/glutamate antiporter: a mediator of pancreatic cancer growth with a role in drug resistance. Br J Cancer 99:464–472. https://doi.org/10.1038/sj.bjc.6604485
21. Habib E, Linher-Melville K, Lin H-X, Singh G (2015) Expression of xCT and activity of system xc(-) are regulated by NRF2 in human breast cancer cells in response to oxidative stress. Redox Biol 5:33–42. https://doi.org/10.1016/j.redox.2015.03.003
22. Ruiu R, Rolih V, Bolli E et al (2018) Fighting breast cancer stem cells through the immune-targeting of the xCT cystine-glutamate antiporter. Cancer Immunol Immunother. https://doi.org/10.1007/s00262-018-2185-1
23. Ye P, Mimura J, Okada T et al (2014) Nrf2- and ATF4-dependent upregulation of xCT modulates the sensitivity of T24 bladder carcinoma cells to proteasome inhibition. Mol Cell Biol 34:3421–3434. https://doi.org/10.1128/MCB.00221-14
24. Ji X, Qian J, Rahman SMJ et al (2018) xCT (SLC7A11)-mediated metabolic reprogramming promotes non-small cell lung cancer progression. Oncogene. https://doi.org/10.1038/s41388-018-0307-z
25. Sugano K, Maeda K, Ohtani H et al (2015) Expression of xCT as a predictor of disease recurrence in patients with colorectal cancer. Anticancer Res 35:677–682
26. Dai L, Noverr MC, Parsons C, et al (2015) xCT, not just an amino-acid transporter: a multi-functional regulator of microbial infection and associated diseases. Front Microbiol 6:. https://doi.org/10.3389/fmicb.2015.00120
27. Okuno S, Sato H, Kuriyama-Matsumura K et al (2003) Role of cystine transport in intracellular glutathione level and cisplatin resistance in human ovarian cancer cell lines. Br J Cancer 88:951–956. https://doi.org/10.1038/sj.bjc.6600786
28. Yang P, Ebbert JO, Sun Z, Weinshilboum RM (2006) Role of the glutathione metabolic pathway in lung cancer treatment and prognosis: a review. J Clin Oncol 24:1761–1769. https://doi.org/10.1200/JCO.2005.02.7110
29. Kaleeba JAR, Berger EA (2006) Kaposi's sarcoma-associated herpesvirus fusion-entry receptor: cystine transporter xCT. Science 311:1921–1924. https://doi.org/10.1126/science.1120878
30. Qin Z, Freitas E, Sullivan R et al (2010) Upregulation of xCT by KSHV-encoded microRNAs facilitates KSHV dissemination and persistence in an environment of oxidative stress. PLoS Pathog 6:e1000742. https://doi.org/10.1371/journal.ppat.1000742
31. Chandran B (2010) Early Events in Kaposi's sarcoma-associated herpesvirus infection of target cells. J Virol 84:2188–2199. https://doi.org/10.1128/JVI.01334-09
32. Dai Z, Huang Y, Sadee W, Blower P (2007) Chemoinformatics analysis identifies cytotoxic compounds susceptible to chemoresistance mediated by glutathione and cystine/glutamate transport system xc. J Med Chem 50:1896–1906. https://doi.org/10.1021/jm060960h
33. Dai L, Noverr MC, Parsons C, et al (2015) xCT, not just an amino-acid transporter: a multi-functional regulator of microbial infection and associated diseases. Front Microbiol 6:. https://doi.org/10.3389/fmicb.2015.00120
34. Shin C-S, Mishra P, Watrous JD et al (2017) The glutamate/cystine xCT antiporter antagonizes glutamine metabolism and reduces nutrient flexibility. Nat Commun 8:15074. https://doi.org/10.1038/ncomms15074
35. Koppula P, Zhang Y, Zhuang L, Gan B (2018) Amino acid transporter SLC7A11/xCT at the crossroads of regulating redox homeostasis and nutrient dependency of cancer. Cancer Commun (Lond) 38:12. https://doi.org/10.1186/s40880-018-0288-x
36. Lewerenz J, Albrecht P, Tien M-LT et al (2009) Induction of Nrf2 and xCT are involved in the action of the neuroprotective antibiotic ceftriaxone in vitro. J Neurochem 111:332–343. https://doi.org/10.1111/j.1471-4159.2009.06347.x
37. Savaskan NE, Fan Z, Broggini T et al (2015) Neurodegeneration in the brain tumor microenvironment: glutamate in the limelight. Curr

Neuropharmacol 13:258–265. https://doi.org/10.2174/1570159X13666150122224158
38. Gout PW, Buckley AR, Simms CR, Bruchovsky N (2001) Sulfasalazine, a potent suppressor of lymphoma growth by inhibition of the x(c)- cystine transporter: a new action for an old drug. Leukemia 15:1633–1640
39. Sehm T, Fan Z, Ghoochani A et al (2016) Sulfasalazine impacts on ferroptotic cell death and alleviates the tumor microenvironment and glioma-induced brain edema. Oncotarget 7:36021–36033. https://doi.org/10.18632/oncotarget.8651
40. Gasol E, Jiménez-Vidal M, Chillarón J et al (2004) Membrane topology of system Xc- light subunit reveals a re-entrant loop with substrate-restricted accessibility. J Biol Chem 279:31228–31236. https://doi.org/10.1074/jbc.M402428200
41. Jiménez-Vidal M, Gasol E, Zorzano A et al (2004) Thiol modification of cysteine 327 in the eighth transmembrane domain of the light subunit xCT of the heteromeric cystine/glutamate antiporter suggests close proximity to the substrate binding site/permeation pathway. J Biol Chem 279:11214–11221. https://doi.org/10.1074/jbc.M309866200
42. Kim JY, Kanai Y, Chairoungdua A et al (2001) Human cystine/glutamate transporter: cDNA cloning and upregulation by oxidative stress in glioma cells. Biochim Biophys Acta Biomembr 1512:335–344. https://doi.org/10.1016/S0005-2736(01)00338-8
43. Deshpande AA, Sharma M, Bachhawat AK (2017) Insights into the molecular basis for substrate binding and specificity of the fungal cystine transporter CgCYN1. Biochim Biophys Acta 1859:2259–2268. https://doi.org/10.1016/j.bbamem.2017.08.020
44. Drew D, Boudker O (2016) Shared molecular mechanisms of membrane transporters. Annu Rev Biochem 85:543–572. https://doi.org/10.1146/annurev-biochem-060815-014520
45. Forrest LR, Zhang Y-W, Jacobs MT et al (2008) Mechanism for alternating access in neurotransmitter transporters. Proc Natl Acad Sci U S A 105:10338–10343. https://doi.org/10.1073/pnas.0804659105
46. Latorraca NR, Fastman NM, Venkatakrishnan AJ et al (2017) Mechanism of substrate translocation in an alternating access transporter. Cell 169:96-107.e12. https://doi.org/10.1016/j.cell.2017.03.010
47. LeVine MV, Cuendet MA, Khelashvili G, Weinstein H (2016) Allosteric mechanisms of molecular machines at the membrane: transport by sodium-coupled symporters. Chem Rev 116:6552–6587. https://doi.org/10.1021/acs.chemrev.5b00627
48. Locher KP (2016) Mechanistic diversity in ATP-binding cassette (ABC) transporters. Nat Struct Mol Biol 23:487–493. https://doi.org/10.1038/nsmb.3216
49. Palmgren MG, Nissen P (2011) P-type ATPases. Annu Rev Biophys 40:243–266. https://doi.org/10.1146/annurev.biophys.093008.131331
50. Quistgaard EM, Löw C, Guettou F, Nordlund P (2016) Understanding transport by the major facilitator superfamily (MFS): structures pave the way. Nat Rev Mol Cell Biol 17:123–132. https://doi.org/10.1038/nrm.2015.25
51. Weyand S, Shimamura T, Beckstein O et al (2011) The alternating access mechanism of transport as observed in the sodium-hydantoin transporter Mhp1. J Synchrotron Radiat 18:20–23. https://doi.org/10.1107/S0909049510032449
52. Yan N (2015) Structural biology of the major facilitator superfamily transporters. Annu Rev Biophys 44:257–283. https://doi.org/10.1146/annurev-biophys-060414-033901
53. Jardetzky O (1966) Simple allosteric model for membrane pumps. Nature 211:969–970
54. Mitchell P (1957) A general theory of membrane transport from studies of bacteria. Nature 180:134–136
55. Adelman JL, Ghezzi C, Bisignano P et al (2016) Stochastic steps in secondary active sugar transport. Proc Natl Acad Sci U S A 113:E3960–E3966. https://doi.org/10.1073/pnas.1525378113
56. Dror RO, Dirks RM, Grossman JP et al (2012) Biomolecular simulation: a computational microscope for molecular biology. Annu Rev Biophys 41:429–452. https://doi.org/10.1146/annurev-biophys-042910-155245
57. Faraldo-Gómez JD, Forrest LR (2011) Modeling and simulation of ion-coupled and ATP-driven membrane proteins. Curr Opin Struct Biol 21:173–179. https://doi.org/10.1016/j.sbi.2011.01.013
58. Fukuda M, Takeda H, Kato HE et al (2015) Structural basis for dynamic mechanism of nitrate/nitrite antiport by NarK. Nat Commun 6:7097. https://doi.org/10.1038/ncomms8097
59. Lee S, Swanson JMJ, Voth GA (2016) Multiscale simulations reveal key aspects of the proton transport mechanism in the ClC-ec1 antiporter. Biophys J 110:1334–1345. https://doi.org/10.1016/j.bpj.2016.02.014
60. Li J, Wen P-C, Moradi M, Tajkhorshid E (2015) Computational characterization of structural dynamics underlying function in active membrane transporters. Curr Opin Struct Biol 31:96–105. https://doi.org/10.1016/j.sbi.2015.04.001
61. Watanabe A, Choe S, Chaptal V et al (2010) The mechanism of sodium and substrate release from the binding pocket of vSGLT. Nature 468:988–991. https://doi.org/10.1038/nature09580
62. Dobson L, Reményi I, Tusnády GE (2015) CCTOP: a Consensus Constrained TOPology prediction web server. Nucleic Acids Res 43:W408–W412. https://doi.org/10.1093/nar/gkv451
63. Shaffer PL, Goehring A, Shankaranarayanan A, Gouaux E (2009) Structure and mechanism of a Na+-independent amino acid transporter. Science 325:1010–1014. https://doi.org/10.1126/science.1176088
64. Ilgü H, Jeckelmann J-M, Gapsys V et al (2016) Insights into the molecular basis for substrate binding and specificity of the wild-type L-arginine/agmatine antiporter AdiC. Proc Natl Acad Sci U S A 113:10358–10363. https://doi.org/10.1073/pnas.1605442113
65. Zimmermann L, Stephens A, Nam S-Z et al (2018) A completely reimplemented MPI bioinformatics toolkit with a new HHpred server at its core. J Mol Biol 430:2237–2243. https://doi.org/10.1016/j.jmb.2017.12.007
66. Ma D, Lu P, Yan C et al (2012) Structure and mechanism of a glutamate-GABA antiporter. Nature 483:632–636. https://doi.org/10.1038/nature10917
67. Eswar N, Webb B, Marti-Renom MA, et al (2006) Comparative protein structure modeling using Modeller. Curr Protoc Bioinformatics 0 5:Unit-5.6. https://doi.org/10.1002/0471250953.bi0506s15
68. Jo S, Cheng X, Lee J et al (2017) CHARMM-GUI 10 years for biomolecular modeling and simulation. J Comput Chem 38:1114–1124. https://doi.org/10.1002/jcc.24660
69. Huang J, MacKerell AD (2013) CHARMM36 all-atom additive protein force field: validation based on comparison to NMR data. J Comput Chem 34:2135–2145. https://doi.org/10.1002/jcc.23354
70. Lomize MA, Pogozheva ID, Joo H et al (2012) OPM database and PPM web server: resources for positioning of proteins in membranes. Nucleic Acids Res 40:D370–D376. https://doi.org/10.1093/nar/gkr703
71. Campbell SD, Regina KJ, Kharasch ED (2014) Significance of lipid composition in a blood-brain barrier-mimetic PAMPA assay. J Biomol Screen 19:437–444. https://doi.org/10.1177/1087057113497981
72. Phillips JC, Braun R, Wang W et al (2005) Scalable molecular dynamics with NAMD. J Comput Chem 26:1781–1802. https://doi.org/10.1002/jcc.20289
73. Darden T, York D, Pedersen L (1993) Particle mesh Ewald: An N·log(N) method for Ewald sums in large systems. J Chem Phys 98:10089–10092. https://doi.org/10.1063/1.464397

74. Lovell SC, Davis IW, Arendall WB et al (2003) Structure validation by Calpha geometry: phi,psi and Cbeta deviation. Proteins 50:437–450. https://doi.org/10.1002/prot.10286
75. Trott O, Olson AJ (2010) AutoDock Vina: improving the speed and accuracy of docking with a new scoring function, efficient optimization and multithreading. J Comput Chem 31:455–461. https://doi.org/10.1002/jcc.21334
76. Seeliger D, de Groot BL (2010) Ligand docking and binding site analysis with PyMOL and Autodock/Vina. J Comput Aided Mol Des 24:417–422. https://doi.org/10.1007/s10822-010-9352-6
77. Smart OS, Neduvelil JG, Wang X et al (1996) HOLE: a program for the analysis of the pore dimensions of ion channel structural models. J Mol Graph 14:354–360. https://doi.org/10.1016/S0263-7855(97)00009-X
78. Kim S, Lee J, Jo S et al (2017) CHARMM-GUI ligand reader and modeler for CHARMM force field generation of small molecules. J Comput Chem 38:1879–1886. https://doi.org/10.1002/jcc.24829
79. Humphrey W, Dalke A, Schulten K (1996) VMD: visual molecular dynamics. J Mol Graph 14(33–38):27–28
80. Smart OS, Goodfellow JM, Wallace BA (1993) The pore dimensions of gramicidin A. Biophys J 65:2455–2460
81. Stelzl LS, Fowler PW, Sansom MSP, Beckstein O (2014) Flexible gates generate occluded intermediates in the transport cycle of LacY. J Mol Biol 426:735–751. https://doi.org/10.1016/j.jmb.2013.10.024
82. Michaud-Agrawal N, Denning EJ, Woolf TB, Beckstein O (2011) MD Analysis: a toolkit for the analysis of molecular dynamics simulations. J Comput Chem 32:2319–2327. https://doi.org/10.1002/jcc.21787
83. Roe DR, Cheatham TE (2013) PTRAJ and CPPTRAJ: Software for processing and analysis of molecular dynamics trajectory data. J Chem Theory Comput 9:3084–3095. https://doi.org/10.1021/ct400341p
84. Kollman PA, Massova I, Reyes C et al (2000) Calculating structures and free energies of complex molecules: combining molecular mechanics and continuum models. Acc Chem Res 33:889–897
85. Genheden S, Ryde U (2015) The MM/PBSA and MM/GBSA methods to estimate ligand-binding affinities. Expert Opin Drug Discovery 10:449–461. https://doi.org/10.1517/17460441.2015.1032936
86. Studer G, Biasini M, Schwede T (2014) Assessing the local structural quality of transmembrane protein models using statistical potentials (QMEANBrane). Bioinformatics 30:i505–i511. https://doi.org/10.1093/bioinformatics/btu457
87. Yamashita A, Singh SK, Kawate T et al (2005) Crystal structure of a bacterial homologue of Na+/Cl–dependent neurotransmitter transporters. Nature 437:215–223. https://doi.org/10.1038/nature03978
88. Cheng MH, Bahar I (2014) Complete mapping of substrate translocation highlights the role of LeuT N-terminal segment in regulating transport cycle. PLoS Comput Biol 10:e1003879. https://doi.org/10.1371/journal.pcbi.1003879
89. Sonne J, Kandt C, Peters GH et al (2007) Simulation of the coupling between nucleotide binding and transmembrane domains in the ATP binding cassette transporter BtuCD. Biophys J 92:2727–2734. https://doi.org/10.1529/biophysj.106.097972
90. Selvam B, Yu Y-C, Chen L-Q, Shukla D (2019) Molecular basis of the glucose transport mechanism in plants. ACS Cent Sci 5:1085–1096. https://doi.org/10.1021/acscentsci.9b00252
91. Coudray NL, Seyler S, Lasala R et al (2017) Structure of the SLC4 transporter Bor1p in an inward-facing conformation. Protein Sci 26:130–145. https://doi.org/10.1002/pro.3061
92. Cain NE, Kaiser CA (2011) Transport activity–dependent intracellular sorting of the yeast general amino acid permease. Mol Biol Cell 22:1919–1929. https://doi.org/10.1091/mbc.E10-10-0800
93. Ghaddar K, Krammer E-M, Mihajlovic N et al (2014) Converting the yeast arginine can1 permease to a lysine permease. J Biol Chem 289:7232–7246. https://doi.org/10.1074/jbc.M113.525915
94. Deshpande AA, Sharma M, Bachhawat AK (2017) Insights into the molecular basis for substrate binding and specificity of the fungal cystine transporter CgCYN1. Biochim Biophys Acta Biomembr 1859:2259–2268. https://doi.org/10.1016/j.bbamem.2017.08.020
95. Bridges RJ, Natale NR, Patel SA (2012) System xc- cystine/glutamate antiporter: an update on molecular pharmacology and roles within the CNS. Br J Pharmacol 165:20–34. https://doi.org/10.1111/j.1476-5381.2011.01480.x